Optimization of Injected Dose Based on Noise Equivalent Count Rates for 2- and 3-Dimensional Whole-Body PET

Carole Lartizien, PhD[1,2]; Claude Comtat, PhD[1]; Paul E. Kinahan, PhD[3]; Nuno Ferreira, PhD[1]; Bernard Bendriem, PhD[1,4]; and Régine Trébossen, PhD[1]

[1]Service Hospitalier Frédéric Joliot, Commissariat à l'Energie Atomique, Orsay, France; [2]Department of Radiology, University of Pittsburgh, Pittsburgh, Pennsylvania; [3]Imaging Research Laboratory, Department of Radiology, University of Washington, Seattle, Washington; and [4]CTI, Knoxville, Tennessee

The noise equivalent count (NEC) rate index is used to derive guidelines on the optimal injected dose to the patient for 2-dimensional (2D) and 3-dimensional (3D) whole-body PET acquisitions. **Methods:** We performed 2D and 3D whole-body acquisitions of an anthropomorphic phantom modeling the conditions for ^{18}F-FDG PET of the torso and measured the NEC rates for different activity levels for several organs of interest. The correlations between count rates measured from the phantom and those from a series of whole-body patient scans were then analyzed. This analysis allowed validation of our approach and estimation of the injected dose that maximizes NEC rate as a function of patient morphology for both acquisition modes. **Results:** Variations of the phantom and patient prompt and random coincidence rates as a function of single-photon rates correlated well. On the basis of these correlations, we demonstrated that the patient NEC rate can be predicted for a given single-photon rate. Finally, we determined that patient single-photon rates correlated with the mean dose per weight at acquisition start when normalized by the body mass index. This correlation allows modifying the injected dose as a function of patient body mass index to reach the peak NEC rate in 3D mode. Conversely, we found that the peak NEC rates were never reached in 2D mode within an acceptable range of injected dose. **Conclusion:** The injected dose was adapted to patient morphology for 2D and 3D whole-body acquisitions using the NEC rate as a figure of merit of the statistical quality of the sinogram data. This study is a first step toward a more comprehensive comparison of the image quality obtained using both acquisition modes.

Key Words: PET; whole-body acquisitions; noise equivalent count rate

J Nucl Med 2002; 43:1268–1278

Oncology imaging using PET with ^{18}F-FDG, a glucose analog, has proven to be effective in evaluating the extent of disease for several types of cancer (*1*). Multibed whole-body PET protocols usually specify short acquisitions, typically 5–10 min at each bed position, to minimize patient discomfort and increase throughput (*2*). The resulting whole-body images are typically characterized by high levels of statistical noise that limit image quality. PET scanners with retractable septa have the possibility of allowing higher-sensitivity 3-dimensional (3D) acquisitions. In 3D mode, the increased sensitivity to true events is partially offset by the higher sensitivity to scattered and random coincidences, particularly random coincidences arising from activity distribution outside the axial field of view (FOV) (*3,4*). Consequently, the overall advantage of 2-dimensional (2D) versus 3D PET whole-body imaging is unclear. An additional complication is that the optimal levels of performance in each mode, as determined by some measure of sinogram or image quality, likely occur at different injected-activity levels.

The aim of this study was to derive guidelines on the activity level of the radiotracer (dose) that should be injected into the patient to optimize the statistical quality of the data for 2D and 3D whole-body PET acquisitions. For that purpose, we used the noise equivalent count (NEC) rate (*5*) as a figure of merit. This issue was not addressed on replicate patient datasets because of ethical considerations. Instead, an anthropomorphic phantom was used to mimic realistic whole-body ^{18}F-FDG PET imaging conditions for the torso. We performed 2D and 3D whole-body acquisitions of the phantom on an ECAT EXACT HR+ scanner (CTI, Knoxville, TN/Siemens Medical Systems, Inc., Hoffman Estates, IL) (*6,7*) and measured NEC rates for different activity levels for several organs of interest. Then, we compared count rates measured from the anthropomorphic phantom and from a series of clinical patient scans to extrapolate results from this phantom experiment to clinical practice. Good correlations between the phantom and the patient scans were obtained for prompt and delayed coincidence count rates measured over the FOV as a function of the single-photon rate. We then demonstrated that the NEC index can be approximated as a function of the total prompt and delayed count rates over the FOV on the basis of the

Received Aug. 6, 2001; revision accepted May 9, 2002.

For correspondence or reprints contact: Carole Lartizien, PhD, CERMEP, Hôpital Neuro-Cardiologique, 59, Boulevard Pinel, 69003 Lyon, France.
E-mail: clartizien@netcourrier.com

assumptions explained below. Using the measurements obtained from the whole-body phantom over a large range of activity, we fitted polynomial models to the prompt and delayed coincidence rates as a function of single-photon rate, allowing us to derive an expression of the patient NEC rate as a function of the single-photon rate. Finally, we demonstrated a good correlation between the patient single-photon rate and the mean dose per weight at acquisition start normalized by the body mass index (BMI). This allowed estimation of the patient NEC rate as a function of the injected dose and BMI. Conversely, it also allowed estimation of the injected dose that maximized the NEC rate as a function of patient height and weight.

The NEC index has been widely used to compare scanner performance for brain imaging (*8–10*). More recently, the NEC performance of different scanners has been investigated for whole-body imaging based on phantom or patient data (*11–13*). The originality of our work, compared with previous studies, is the use of a realistic model of ^{18}F-FDG distribution in the human torso, in particular accounting for accurate activity distribution outside the FOV, which can significantly affect the NEC rate. Moreover, by investigating correlations between phantom and patient studies, we were able to demonstrate the consistency of our model and to extrapolate results to clinical practice.

MATERIALS AND METHODS

The definitions of symbols used here are summarized in Table 1.

Phantoms and Data Acquisition

The anthropomorphic phantom (Radiologic Support Device Inc., Long Beach, CA) contains heart, lung, and liver compartments that can be filled separately. These components have attenuation coefficients equivalent to human tissues at 511 keV (*14*). A head phantom (Radiologic Support Device Inc.) was attached to the torso as well as 2 fillable acrylic cylinders (arms) and a serum bag (bladder) to complete the human model. The different compartments of the phantom were filled with dilute ^{18}F, and the ratio of the activity concentration in each organ to the activity concentration in the thoracic cavity matched typical clinical ratios (Table 2). These values were obtained from regions of interest drawn on patient images and agreed well with values reported in the literature (*14–16*).

The experiment was performed on the ECAT EXACT HR+ scanner (*6,7*). This scanner consists of 32 rings of bismuth germanate detectors with an axial FOV of 15.5 cm. The data were acquired in 3D and 2D modes with an energy window from 350 to 650 keV and a maximum acceptance angle of 4° in 2D mode (equivalent to a ring difference of 7) and 12.5° in 3D mode (ring difference of 22). The lines of response (LORs) were compressed axially into groups of 7 or 8 LORs in 2D mode and of 4 or 5 LORs in 3D mode (*17*). Whole-body acquisitions of 2 min per bed position were performed using 6 bed positions. The overlap between bed positions was set to 12 planes corresponding to 26.7 mm for both acquisition modes, which is the default value for 3D acquisitions. The scanning protocol (Fig. 1) consisted of a 2D whole-body scan immediately followed by a 3D whole-body scan. This 2D–3D sequence was repeated 14 times over 15 half-lives of the radiotracer, allowing for comparison of 3D and 2D acquisitions over a wide range of activity concentrations. The phantom was filled with 700 MBq of aqueous ^{18}F at the beginning of the first scan. A 15-min transmission scan per bed position was performed at the end of the emission protocol.

TABLE 1
Symbol Definitions

Symbol	Definition
T	True coincidence count rate (kcps)
S	Scattered coincidence count rate (kcps)
R	Random coincidence count rate (kcps)
P	Prompt coincidence count rate, defined as $P = T + S + R$
D	Delayed coincidence rate, defined as $D = R$
σs	Scatter fraction, defined as $\sigma s = S/(T + S)$
SP	Single-photon count rate (Mcps)
NEC	Noise equivalent count rate (kcps)
A	Activity concentration (kBq/mL) in phantom thoracic chamber
d	Mean tracer activity in patient at acquisition start (MBq)
c	Mean activity per weight d/w
$\hat{c}$	Mean activity in patient normalized for patient morphology
α	Proportionality constant in $SP = \alpha \cdot A$ (Eq. 1)
β and $\hat{\beta}$	Proportionality constant in $SP = \beta \cdot c$ and $SP = \beta \cdot \hat{c}$ (Eqs. 8 and 9)
w	Patient weight (kg)
h	Patient height (m)
BMI	Body mass index, defined as BMI $= w/h^2$

Count Rate Measurements

The rates of random, scattered, and true coincidences and the rate of single photons were obtained as a function of the mean activity concentration A in the thoracic chamber of the phantom for acquisitions centered on the brain, the thorax, and the abdomen.

The rate of random coincidences was measured using a delayed coincidence window. The transmission scan was used to determine the fraction of the FOV f subtended by the phantom to determine the rate of random coincidences R within the object boundaries.

To account for the effect of activity sources outside the FOV, we estimated the scatter distribution in each acquisition mode using the method of Cherry et al. (*18*) based on the comparison of the 2D and 3D sinograms of the direct planes. The sinograms acquired in 2D mode were corrected for detector efficiency variations and then corrected for scatter using the 1-dimensional deconvolution method of Bergström et al. (*19*). The resulting sinograms were considered as the reference for the distribution of true coincidences. The 2D and 3D scatter sinograms were calculated by subtracting this reference from the 2D and 3D emission sinograms after efficiency normalization and correction for isotope decay for the 3D acquisitions. The transmission scan was used to define an object mask that was applied to the sinograms to determine the rate of scattered coincidences S within the phantom boundaries.

Finally, the true event rate T was calculated from the prompt coincidence rate (sum of the true, scattered, and random coincidences) by subtracting the scatter sinograms derived previously and the delayed coincidences.

TABLE 2
Volumes and Contrasts of Different Organ Compartments of Phantom

Inserted organ	Volume (mL)	Contrast*
Thoracic chamber	7,500	1
Heart	236	5
Brain	1,100	5
Left lung	848	1
Right lung	1,137	1
Arms	453	1
Liver	1,008	3
Bladder	250	15

*Defined as ratio of activity concentration in organ to activity concentration in thoracic chamber.

We used a linear function to fit the variations of the single-photon rate *SP* as a function of the activity concentration *A* for data points at which the dead time was negligible and for acquisitions centered on the thorax and abdomen. This determined the parameters α_{2D} and α_{3D} in:

$$SP_{2D} = \alpha_{2D} \cdot A \quad \text{and} \quad SP_{3D} = \alpha_{3D} \cdot A. \qquad \text{Eq. 1}$$

Deviations from the linearity of Equation 1 will occur because of scanner dead-time effects. The dead-time effect on the single-photon rate was measured by comparing the fitted and measured single-photon rates at higher activity levels. The same methodology was used to estimate the dead time for the true coincidence rates.

NEC Calculation

The NEC rate formula is defined (Eq. 7 of Strother et al. (*5*)), for the case of noiseless scatter correction, as:

$$\text{NEC} = \frac{T^2}{(T + S + 2R)}, \qquad \text{Eq. 2}$$

where *T*, *S*, and *R* are the rates of true, scattered, and random coincidences within the boundaries of the object scanned. The variance term due to random coincidences is doubled, as the random coincidence rates were estimated using a delayed coincidence method (*5*).

Using Equation 2 and the phantom count rates measured as described in the previous section, we calculated the NEC rates in 2D and 3D modes for acquisitions centered on the brain, thorax, and abdomen of the whole-body phantom as a function of the activity *A*.

Estimation of Patient NEC Rates as a Function of Single-Photon Rates

For the patient studies, we express the NEC rate in terms of the directly measured prompt coincidence rate $P = T_{FOV} + S_{FOV} + R_{FOV}$ (where T_{FOV}, S_{FOV}, and R_{FOV} are, respectively, the true, scattered, and random coincidences measured over the entire FOV), the delayed coincidence rate $D = R_{FOV}$, and the scatter fraction $\sigma s = S/(S + T)$. Because $T = T_{FOV}$ and $R = fR_{FOV}$, and if we approximate $S \cong S_{FOV}$ as is typically done by assuming a forward peaked scatter distribution (*5*,*8*,*20*), we can write:

$$\text{NEC} = (1 - \sigma s_{FOV})^2 \frac{(P - D)^2}{(P + (2f - 1)D)}, \qquad \text{Eq. 3}$$

where σs_{FOV} is the scatter fraction using the entire scanner FOV, defined as $\sigma s_{FOV} = S_{FOV}/(S_{FOV} + T)$. A result similar to Equation 3 was derived by Barnes et al. (*20*) for brain imaging applications. Because $S < S_{FOV}$, the estimated NEC rates are reduced compared with those that would be measured following the NU 2-2000 standards of the National Electrical Manufacturers Association ([NEMA] Rosslyn, VA) (*21*). This does not, however, significantly affect the location of the peak NEC rate with respect to activity in the phantom or patient. This expression of the NEC rate depends on, first, the activity distribution that determines the count rates *P* and *D* and, second, the terms *f* and σs_{FOV} that depend on patient morphology.

To estimate NEC rates for patient studies, we examined the correlation of the prompt and delayed coincidence rates and single-photon rates between the phantom and patient datasets following the method of Smith et al. (*13*). Two bed positions centered on the thorax and abdomen were selected for comparison. Twenty-one 3D whole-body scans (14 male, 7 female) and ten 2D whole-body scans (3 male, 7 female) of clinical oncology patients were selected on the criterion that they matched the positions of the anthropomorphic phantom organs inside and outside the FOV. PET was performed as part of research protocols approved by local ethical review committees. Patient body weights averaged 67 ± 13 kg and ranged from 45 to 90 kg. Patient heights averaged 170 ± 9 cm and ranged from 150 to 182 cm. For both patient height and patient weight, median values were not significantly different from average values. Patients received a dose corresponding to approximately 3.7 MBq/kg (100 μCi/kg) and were scanned 1 h after injection. The mean activity concentration in the patients at the start of scanning was 2.5 ± 0.5 MBq/kg (67 ± 14 μCi/kg). To estimate the fraction *f* of the FOV subtended by the patient cross-sectional shape, the semiaxis values of each patient's torso were measured on transaxial slices of the emission scan of the thorax, assuming an elliptic shape. The mean values were 110 ± 11 mm for the semiminor axis and 148 ± 11 mm for the semimajor axis of the ellipse. The fraction *f* was then numerically computed for each patient considering only the LORs perpendicular to the scanner axis (no oblique LORs). This gave a mean fraction *f* of 0.47 ± 0.04.

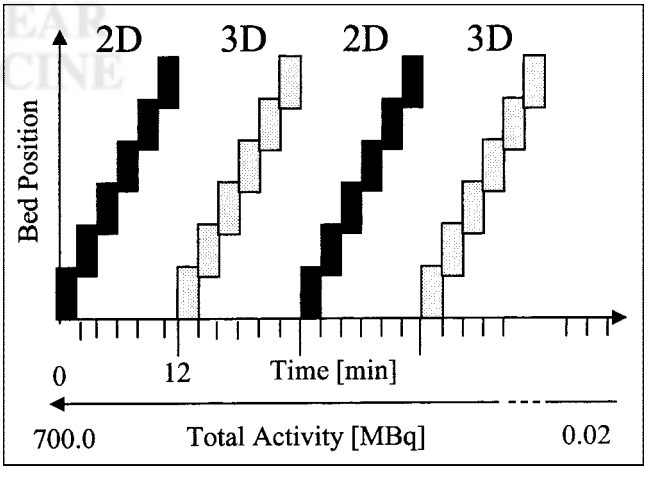

FIGURE 1. Acquisition protocol schematic showing interleaving of 2D and 3D acquisitions for each bed position.

On the basis of the method of Smith et al. (*13*), the variations of the prompt and random coincidence rate over the FOV as a function of the single-photon rate were plotted for the phantom and patient datasets. As shown in the Results, we found that curves for the phantom and patients were superimposed. This allowed us to use the phantom count rates measured over a large range of activity, unlike patient data, to adjust a polynomial model to the variations of the prompt coincidence rate P as a function of the single-photon rate SP and derive the function h in:

$$P = h(SP). \qquad \text{Eq. 4}$$

To determine patient NEC rate, we also confirmed that the delayed coincidence rate D is fully determined by the single-photon rate as:

$$D = 2\tau s SP^2, \qquad \text{Eq. 5}$$

where $2\tau s$ is a proportionality constant accounting for the scanner sensitivity (s) and the coincidence time window (2τ) (*22*).

Substituting P and D in Equation 3 by their expression as a function of the single-photon rate in Equations 4 and 5 gives:

$$\text{NEC} = (1 - \sigma s_{FOV})^2 \frac{(h(SP) - 2\tau s SP^2)^2}{h(SP) + (2f - 1)(2\tau s SP^2)}. \qquad \text{Eq. 6}$$

Equation 6 allows predicting the patient NEC rate as a function of single-photon rate by determining the function h in Equation 4 and the proportionality constant $2\tau s$ in Equation 5 from the measured phantom data. This, however, requires fixing the parameters f and σs_{FOV}. Based on our series of patients, we found that f ranged from 0.43 to 0.51. To estimate the influence of this factor on the NEC rate, the NEC curves were plotted with f set to these 2 extreme values. Results indicated that f had no significant effect on the location of the peak NEC rate, which is the main point of interest in this study. Thus, f was considered as a constant set to the estimated average value of 0.47. Similarly, Equation 6 indicates that uncertainties in the global scale factor $(1 - \sigma s_{FOV})^2$ may affect the magnitude of the NEC rate but not the location of the peak value. Based on these assumptions, the relative patient NEC rate may be expressed as:

$$\text{NEC} = g(SP). \qquad \text{Eq. 7}$$

Then, if we establish a relationship between SP and some index related to the dose injected into the patient, we can derive the variation of the NEC as a function of patient dose.

Single-Photon and NEC Rates as a Function of Patient Dose

We investigated the patient single-photon rates as a function of the dose per weight d/w, where w is the patient weight in kg and d is the injected dose in megabecquerels corrected for the delay between the injection and the acquisition. A linear regression was applied to the variation of the 3D single-photon rate SP_{3D} as a function of the mean activity per weight similar to Equation 1:

$$SP_{3D} = \beta_{3D} \cdot c, \qquad \text{Eq. 8}$$

where $c = d/w$.

To improve the correlation between SP_{3D} and c by accounting for differences in habitus, which influences attenuation, we also normalized c by the relative BMI (*23*,*24*):

$$SP_{3D} = \hat{\beta}_{3D} \cdot \hat{c}, \qquad \text{Eq. 9}$$

where $\hat{c} = c \cdot (\text{BMI}/\langle\text{BMI}\rangle)$ and $\langle\text{BMI}\rangle$ is the average BMI corresponding to a 70-kg and 170-cm-tall patient ($\langle\text{BMI}\rangle = 24.2$ kg/m^2). The BMI index is used as a general measure of obesity and was calculated as BMI $= w/h^2$, where h is the patient height in meters.

The correlations between the 2D single-photon rate SP_{2D} and the activity concentrations c and $\hat{c}$ were not derived from the set of 2D clinical data because of the small sample size (10 patients). Instead, these correlations were derived from those measured on the 3D datasets, assuming that the geometric similarity between the phantom and patient studies with respect to single-photon rate allows us to write $\frac{\alpha_{2D}}{\alpha_{3D}} = \frac{\beta_{2D}}{\beta_{3D}} = \frac{\hat{\beta}_{2D}}{\hat{\beta}_{3D}}$ and, thus,

$$\beta_{2D} = \frac{\alpha_{2D}}{\alpha_{3D}} \beta_{3D} \quad \text{and} \quad \hat{\beta}_{2D} = \frac{\alpha_{2D}}{\alpha_{3D}} \hat{\beta}_{3D}. \qquad \text{Eq. 10}$$

The combination of Equations 7 and 9 gives the predicted NEC rate as a function of $\hat{c}$:

$$\text{NEC} = g(\hat{\beta} \cdot \hat{c}). \qquad \text{Eq. 11}$$

This allows estimating the injected dose that maximizes NEC rate for both 2D and 3D acquisitions as a function of patient height and weight.

RESULTS

Figure 2 shows representative images of the reconstructed distribution of activity in the phantom. These images correspond to PET acquisitions of 2 min per bed position. For the results presented below, we did not consider the lower extremities of the first and last bed positions, corresponding, respectively, to the acrylic neck and pedestal of the phantom.

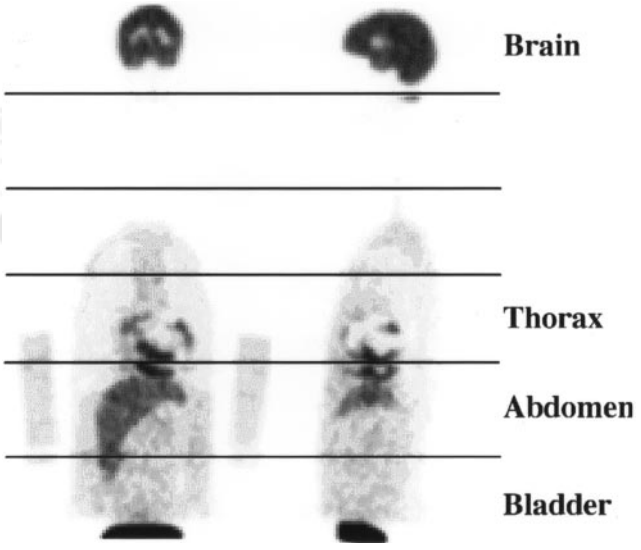

FIGURE 2. Representative PET images of whole-body phantom corresponding to acquisitions of 2 min per bed position (coronal view [left] and sagittal view [right]). Horizontal lines indicate limits of different bed positions. Note bed overlap seen between first 2 bed positions.

TABLE 3
Percentage Scatter Fractions for Bed Positions Centered on Main Organs of Interest and for 20-cm-Diameter Cylinder

Acquisition mode	Brain		Thorax		Abdomen		Cylinder
	Obj	FOV	Obj	FOV	Obj	FOV	(Obj)
2D	9	19	14	20	14	20	10
3D	25	32	51	56	45	51	31

Obj = within object; FOV = over entire FOV.

Count Rate Measurements

Table 3 reports the estimated 2D and 3D scatter fractions within the object and for the entire FOV. Values for the torso were almost constant among the different bed positions, with the 2D and 3D values being approximately 20% and 55%. For comparison with published values (*6*), the same calculations were made from 2D and 3D scans of a 20-cm-diameter cylinder filled with ^{68}Ge.

Figure 3 shows the single-photon rates and the coincidence rates within the phantom as a function of the mean activity concentration A in the thoracic chamber obtained in 2D and 3D modes. The main results presented in Figure 3 are, first, that the 3D count rates are considerably higher than the 2D count rates for the same activity level and, second, that the random fractions are considerably higher in the torso than in the brain. In particular, the random coincidence rate in 3D mode exceeds the true coincidence rate for $A > 6$ kBq/mL for the thorax and the abdomen.

For low values of the activity concentration A, the 2D and 3D single-photon rates varied linearly as a function of A. These curves were fitted using a linear function to determine α_{2D} and α_{3D} in Equation 1. These parameters (in units of Mcps/kBq/mL) for the thorax and abdomen were, respectively, 0.32 and 0.47 in 2D mode and 1.16 and 1.54 in 3D mode. By comparing the fitted and the measured single-photon rates, we found that the dead time for 2D mode single-photon rates was negligible over the range of activity concentration considered in this study (maximum activity concentration A of 25 kBq/mL). The corresponding dead-time fractions for the 3D single-photon rates are reported in Table 4.

The true coincidence dead time was estimated using the same method. The dead time for 2D acquisitions centered on the thorax and the abdomen reached 5% for an activity concentration of 15 kBq/mL in the thoracic chamber and 10% for a concentration of 20 kBq/mL. The estimated 3D acquisition dead times are given in Table 5.

NEC Calculation

Figure 4 shows the NEC rates measured in 2D and 3D modes as a function of the mean activity A in the phantom thoracic chamber.

As expected, the NEC rate measured for the brain was significantly higher in 3D than 2D mode at any activity level. The maximum value of the NEC rate in the object was 275 kcps in 3D mode (Fig. 4A) for an activity concentration A of 25 kBq/mL, corresponding to an activity concentration of 125 kBq/mL in the brain, based on the contrast of 5:1 between the brain and the thoracic chamber (Table 1). In 2D mode, the NEC rate measured over the brain increased almost linearly with A within the examined range.

For the torso, the NEC rates measured in 3D mode were higher than the 2D values up to an activity concentration A of 10 kBq/mL for the thorax and 11.5 kBq/ml for the abdomen (Figs. 4B and 4C). The maximum 3D NEC rates were obtained for an activity concentration of 9 kBq/mL for the thorax and 7 kBq/mL for the abdomen. The true coincidence dead times at the peak 3D NEC rate were 10% for the thorax and 13% for the abdomen. The corresponding single-photon dead times were 3% for the thorax and 4% for the abdomen.

Estimation of Patient NEC Rates as a Function of Single-Photon Rates

Figure 5 compares the variations of the prompt and random coincidence rates over the FOV as a function of the single-photon rates measured for the anthropomorphic phantom data and the clinical datasets in 2D and 3D modes for bed positions centered on the thorax and abdomen. Patient and phantom data in 3D mode were superimposed for single-photon rates between 5 and 9 Mcps, corresponding to an activity concentration A ranging from 2.5 to 9.5 kBq/mL. In 2D mode, phantom and patient data were superimposed for single-photon rates between 2 and 4 Mcps. Variations of the prompt coincidence rate were well described by a second-order polynomial function. Coefficients of these polynomials are reported in Figures 5A and 5B for 2D acquisitions centered on the thorax and the abdomen, respectively, and in Figures 5C and 5D for 3D acquisitions. This determines the function h in Equation 4. We also verified the validity of Equation 5 for the random coincidence rate. The constant $2\tau s$ was, respectively, 1,220 ns in 2D mode and 2,500 ns in 3D mode.

Single-Photon and NEC Rates as a Function of Patient Dose

Figure 6 shows the variations of the patient single-photon rates for 3D acquisitions, SP_{3D}, as a function of the mean activity per weight at scan start, $c = (d/w)$, and as a function

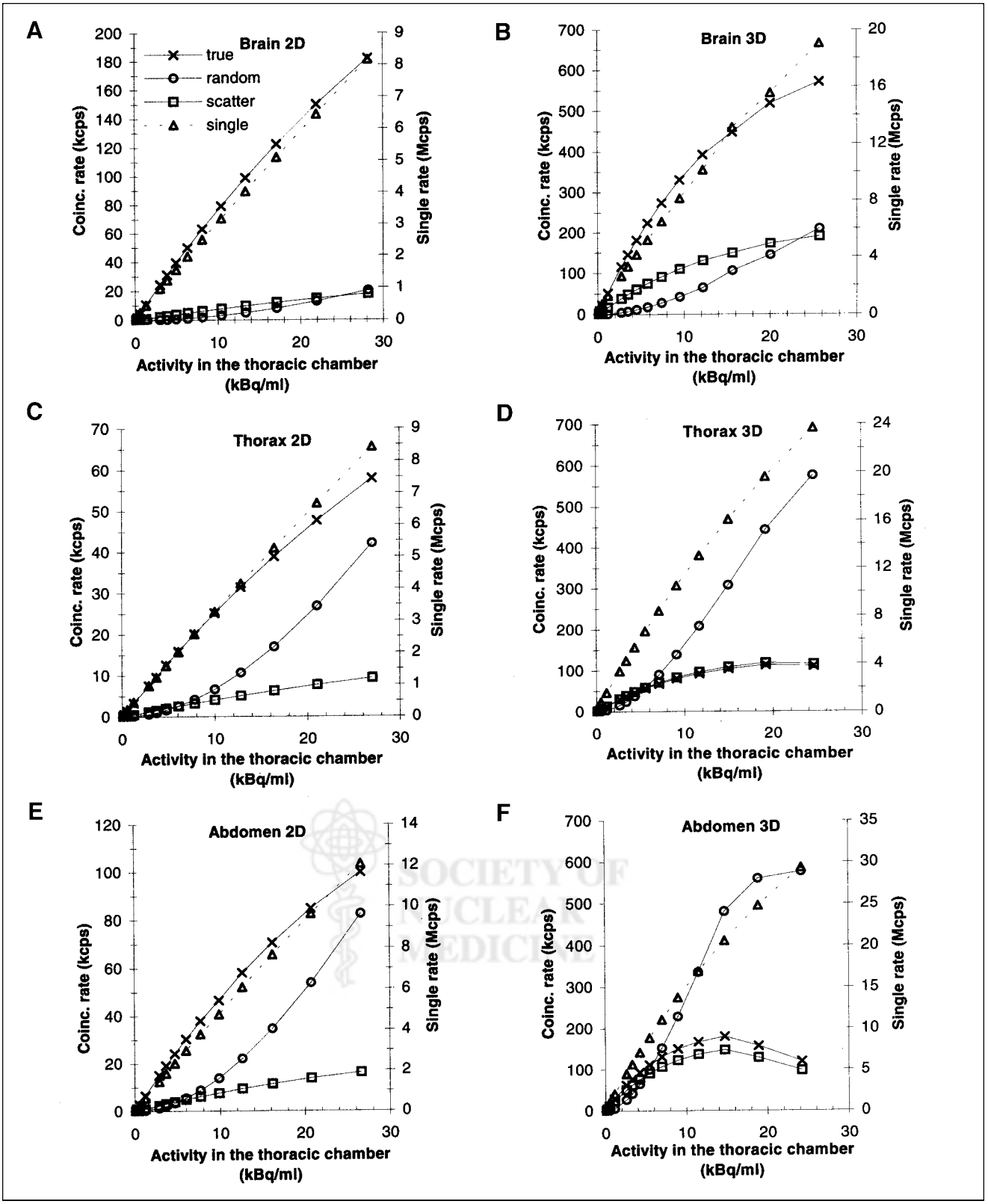

FIGURE 3. Comparison of 2D and 3D count rates for brain (A and B), thorax (C and D), and abdomen (E and F) as function of mean activity concentration in phantom thoracic chamber.

TABLE 4
Percentage Single-Photon Dead-Times, dt_{SP}, for 3D Acquisitions Centered on Thorax and Abdomen

Acquisition site	Parameter	*A* (kBq/mL) 4	8	12	16	20
Thorax	*SP* (Mcps)	5	9	13	17	20
	dt_{SP} (%)	0	3	7	11	15
Abdomen	*SP* (Mcps)	7	12	18	22	25
	dt_{SP} (%)	0	5	11	16	20

of the mean activity per weight corrected for the relative BMI, $\hat{c} = c \cdot (\text{BMI}/\langle\text{BMI}\rangle)$.

The measured patient single-photon rate was generally weakly described as a linear function of the mean activity concentration c with $r^2 = 0.37$ for the thorax and $r^2 = 0.51$ for the abdomen (Figs. 6A and 6C). The correlation coefficient was significantly improved using the mean activity per weight adjusted for the relative BMI, $\hat{c}$, with $r^2 = 0.66$ for the thorax and $r^2 = 0.74$ for the abdomen (Figs. 6B and 6D).

The linear relationship between SP_{3D} and c or $\hat{c}$ in Equations 8 and 9 is valid as long as the dead-time effect on the rate of registered single photons is kept negligible. We found that the single-photon dead time in 3D exceeded 10% for single-photon rates in the thorax and abdomen higher than 17 Mcps (Table 4). This value of 10% single-photon dead time was considered as the upper limit of validity of the linear relationship between SP_{3D} and c or $\hat{c}$.

The proportionality constants $\hat{\beta}_{2D}$ for the thorax and the abdomen were derived from the 3D values using Equation 12. $\hat{\beta}_{2D}$ equaled 0.85 for the thorax and the abdomen.

Estimating Dose Required to Achieve Peak 2D and 3D NEC Rates

Combining Equations 7 and 9, we were then able to predict the 2D and 3D relative NEC variations as a function of $\hat{c}$ on the basis of Equation 11. Figure 7 shows the predicted 2D and 3D NEC rates for the thorax and the abdomen as a function of the dose injected to a standard 70-kg and 170-cm-tall patient (BMI = 24.2 kg/m^2) and assuming a 90-min uptake period. The estimated patient peak NEC rates for the thorax and the abdomen were never reached in 2D mode within the range of activity considered. For 3D acquisitions, the peak NEC rates were achieved for a mean injected dose of 450 MBq (12.2 mCi) for the thorax and of 500 MBq (13.5 mCi) for the abdomen.

Figure 8 reports the variations of the dose per weight at acquisition start that maximizes the peak 3D NEC rate as a function of patient BMI. These curves were obtained by expressing c as a function of SP_{3D} and BMI based on Equation 9 and replacing SP_{3D} by the single-photon rate at the peak 3D NEC rate. The corresponding dose at injection time can be derived by correcting the dose at acquisition time by the decay of the isotope during the chosen uptake period. These curves allow adapting the injected dose to the patient as a function of BMI to achieve the best statistical quality of the data for 3D acquisitions. For an acquisition centered on the abdomen, Figure 8 indicates that the peak 3D NEC rate for a standard patient ($\langle\text{BMI}\rangle$ = 24.2 kg/m^2) would be achieved for a mean starting-time activity of 4.1 MBq/kg. This activity concentration, as previously derived from Figure 7B, corresponds to an injected dose of 500 MBq (13.5 mCi), assuming a 90-min uptake period, or 413 MBq (11.2 mCi) for a 60-min uptake.

DISCUSSION

Our purpose in this study was to replicate as closely as possible clinical whole-body acquisition settings to derive guidelines for optimal 2D and 3D acquisition injection protocols using the NEC index as a figure of merit of the statistical quality of the data. One of the original aspects of this study was the use of a torso phantom to accurately account for the activity distribution inside and outside the axial FOV, because this distribution can strongly affect NEC rates. We measured the NEC index in the phantom for 3 regions of interest (brain, thorax, and abdomen) for both 2D and 3D acquisitions. This model of the human torso was validated by demonstrating the correlation between the prompt and delayed coincidence rates and single-photon rates for the anthropomorphic phantom and for the thorax and abdomen of patients (Fig. 5). This point is a key result of this study, as it allowed predicting the relative NEC variations for a patient as a function of the single-photon rate. We then derived linear relationships between the single-photon rate and the mean dose per weight at acquisition start. The single-photon rate correlated weakly with the activity concentration, $c = d/w$ (Figs. 6A and 6C). The normalization of the dose per weight by the relative BMI, $\hat{c} = c \cdot (\text{BMI}/\langle\text{BMI}\rangle)$, significantly improved the correlation (Figs. 6B and 6D). There was, however, remaining dispersion in the patient single-photon rates expressed as a linear function of $\hat{c}$ for the 21 patients studied. This was likely due to intersubject physiologic and biodistribution variations and urinary excretion. These correlations allowed estimating the injected dose that optimizes the NEC rate for 2D and 3D acquisitions. Results showed that neither of the 2D or 3D acquisition modes performs best overall according to NEC for torso imaging, but relative performance depends on allowable dose and the local imaging environment, which is affected by factors such as the activity outside the axial FOV. The peak 2D NEC rates for the thorax and the

TABLE 5
Percentage True Coincidence Dead-Times, dt_T, for 3D Acquisitions Centered on Thorax and Abdomen

Acquisition site	Parameter	*A* (kBq/mL) 4	8	12	16	20
Thorax	dt_T (%)	0	6	18	30	40
Abdomen	dt_T (%)	2	18	32	46	62

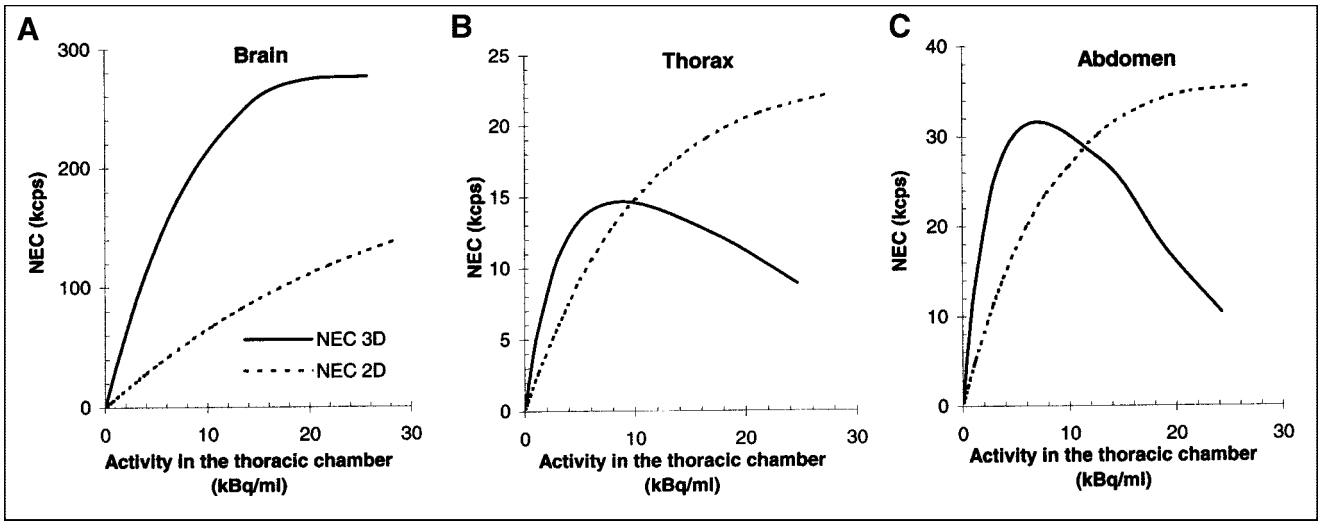

FIGURE 4. Comparison of 2D and 3D NEC rates in phantom and in entire FOV as function of activity concentration in phantom thoracic chamber for brain (A), thorax (B), and abdomen (C).

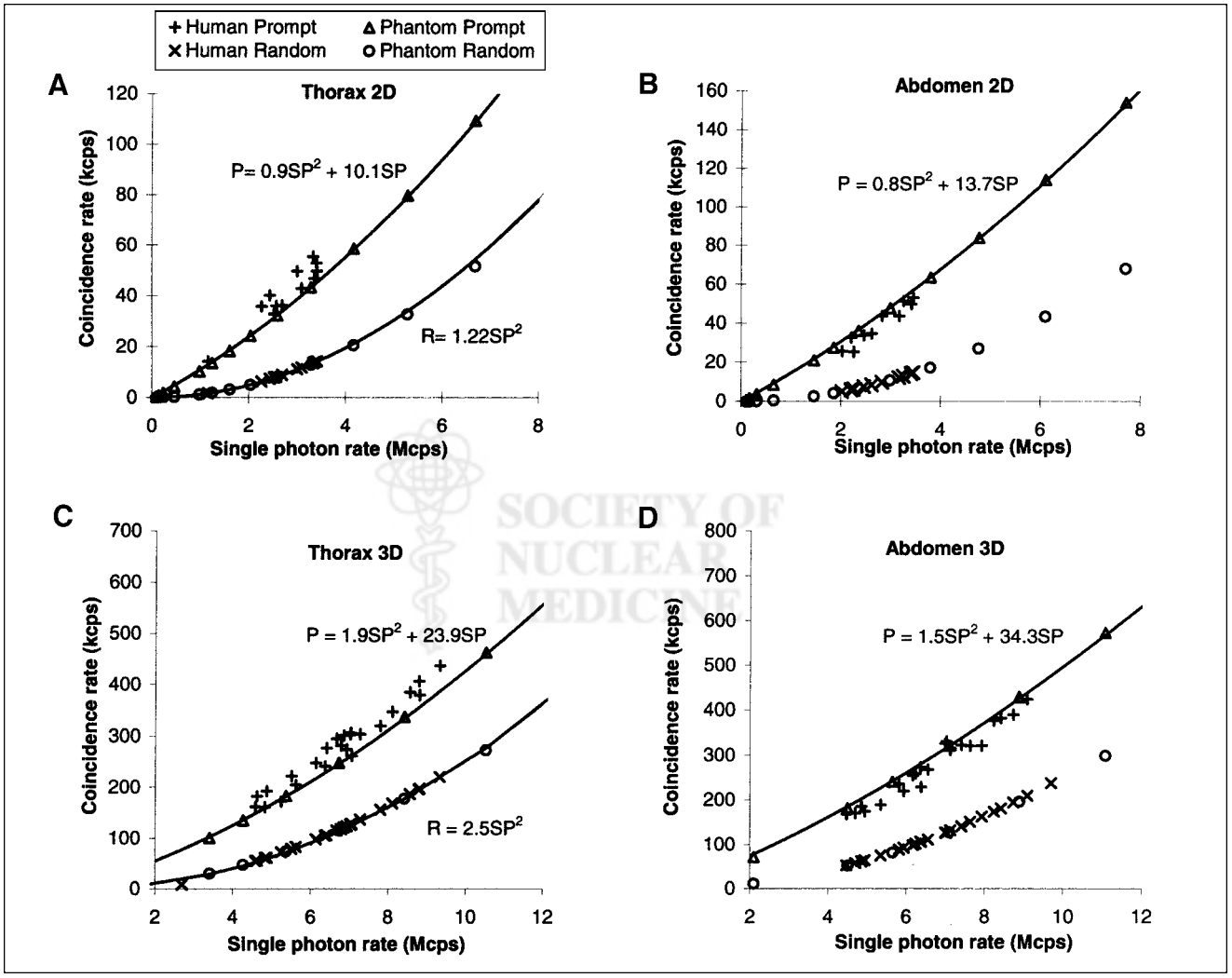

FIGURE 5. Variations of 2D and 3D prompt and random coincidence rates as function of single-photon rates for bed positions centered on thorax (A and C) and abdomen (B and D) for phantom and clinical datasets.

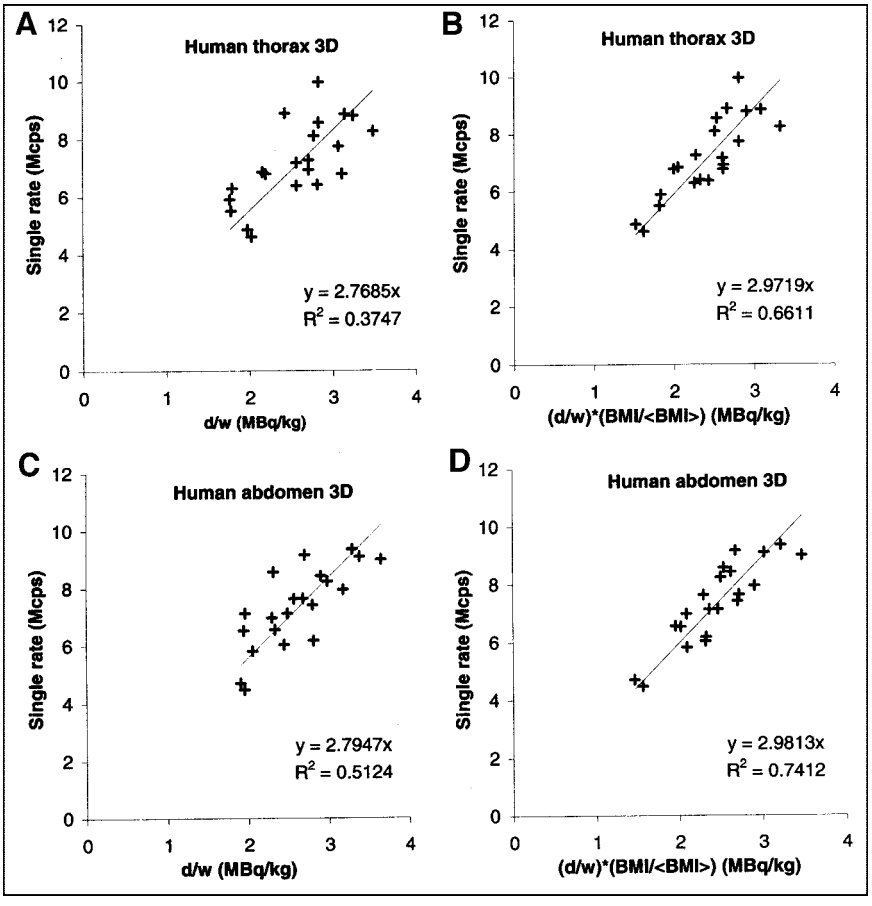

FIGURE 6. Linear regressions for single-photon rates in 3D mode as function of mean dose in patient at scan start for acquisitions centered on thorax and abdomen. Dose is normalized by weight (A and C) and by weight corrected for relative BMI (B and D).

abdomen were never reached within an acceptable range of activity, suggesting that the optimal injected dose in 2D mode according to NEC should be driven by ethical considerations based on the maximal allowable dose delivered to the patient. For 3D acquisitions, the injected dose that optimizes the NEC rate as a function of weight and height is given in Figure 8.

The main limitation to the predicted NEC rate for patients in Figure 7 is that these curves are based on the assumption of the linear relationships between *SP* and *A* in Equation 1 and between *SP* and $\hat{c}$ in Equation 9. These linear relationships become invalid at high activity because of dead-time effects. We chose a 10% single-photon dead time as the upper limit of the linear range. The maximum single-photon dead time in 2D mode was lower than 5% within the range of activity considered in this study, so that we can be confident about the predicted NEC rates for 2D acquisitions (Fig. 7). For 3D acquisitions, the shape of the NEC curves for injected-dose values higher than 710 MBq (19 mCi) should be interpreted with caution, as they correspond to

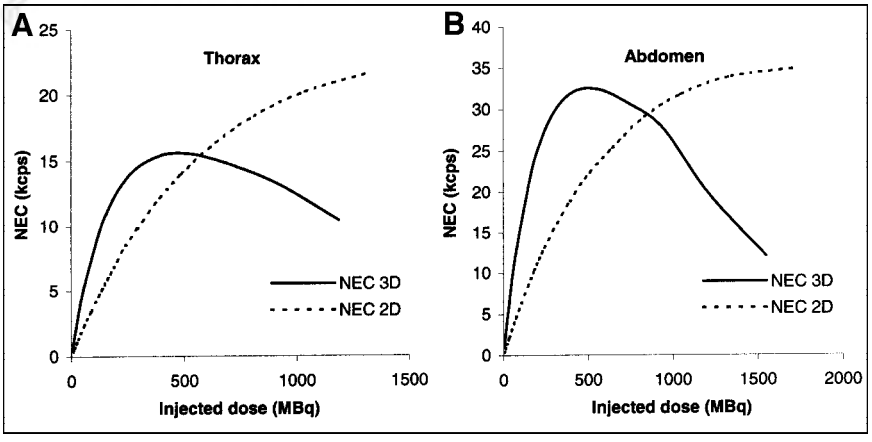

FIGURE 7. Estimated 2D and 3D NEC as function of dose injected to 170-cm and 70-kg patient assuming 90-min uptake period. These curves were obtained for thorax (A) and abdomen (B).

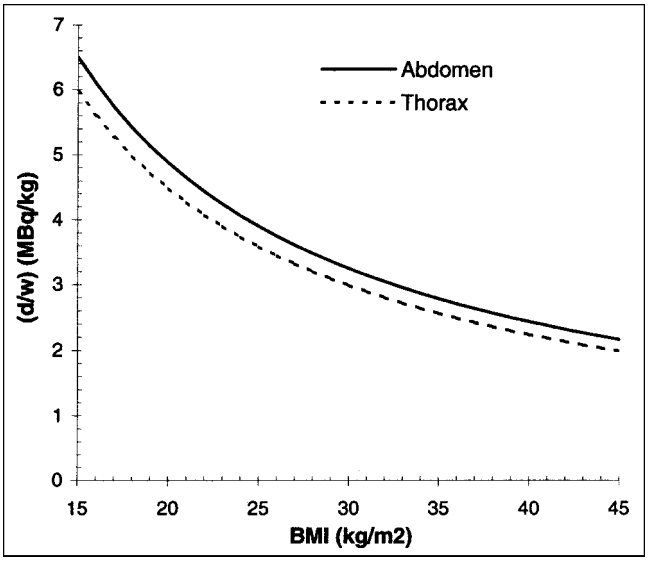

FIGURE 8. Injection rule for 3D acquisition centered on thorax and abdomen as function of patient BMI to achieve peak 3D NEC rate.

single-photon dead times higher than 10%. It is likely that fitting a nonlinear relationship between *SP* and *A* and between *SP* and $\hat{c}$ would improve the accuracy of the predicted NEC rate for this range of elevated dose by accounting for dead-time effects. The peak 3D NEC rate, however, is in the linear range of Equations 1 and 9. As a consequence, the curves of the predicted injected dose per weight as a function of BMI presented in Figure 8 are not affected by dead time.

Another limitation of the predicted NEC rate for patients is the fixed value of the fraction *f* of the FOV subtended by the object. As mentioned in the methods, we estimated the error on the location of the 3D peak NEC rate by plotting the NEC curves corresponding to the 2 extreme values of $f = 0.43$ and $f = 0.51$. The maximum difference in the activity concentration corresponding to the peak NEC rate was less than 5%, thus suggesting that our approximation in fixing the parameter *f* in Equation 6 does not significantly affect the results of this study. The scatter fractions used to estimate the NEC curves in Figure 7 were set to the values measured for the whole-body phantom. Thus, these curves do not provide accurate information on the absolute NEC rates for patients, since this value will depend on the scatter fractions. This scale change, however, will not affect the activity at which the peak NEC rate is reached.

The complex shape of the anthropomorphic phantom did not allow measurement of the scatter fraction with an inserted line source, as recommended by the NEMA procedure (*25*). As a consequence, the scatter fractions for the 20-cm-diameter cylinder in Table 3 differ slightly from the NEMA protocol values (*6*).

The 3D NEC rates for the brain in Figure 4A correlate well with the 3D NEC rate measured for a 10-cm-diameter (1,217 mL) cylinder on an HR+ scanner (*26*), although differences in phantom geometry may explain why the NEC curve for the brain phantom tends to reach the peak NEC rate at a lower activity. Our measurements from the brain phantom also correlate well with those reported by Wienhard et al. (*27*), comparing the ratio of the 3D NEC rates to the 2D NEC rates for cerebral studies on patients, and also with the work of Bailey (*28*) suggesting that 3D acquisitions detect fewer random events than 2D acquisitions for the same rate of true events for brain-type geometries (Figs. 3A and 3B).

The ratios of 3D NEC to 2D NEC for torso imaging were consistent with the NEC ratios of a patient whole-body scan reported by Townsend et al. (*26*) for the HR+ scanner. They also correlated well with the phantom measurements of Laforest et al. (*12*) on the HR+ scanner, suggesting that the peak 3D NEC is achieved for an activity concentration lower than 10 kBq/mL. However, the ratios of 3D to 2D NEC rates were lower in our experiment, and this finding may be explained by differences in the estimated scatter fractions. Discrepancies were observed when our results were compared with those of Badawi et al. (*11*), who reported NEC rates for the ECAT 951 (CTI/Siemens) scanner using the elliptic chest phantom of the European Economic Community, and with the NEC performances reported by Smith et al. (*13*) for the C-PET (ADAC Laboratories/Philips Medical Systems, Inc., Milpitas, CA) scanner based on a 20-cm-diameter by 70-cm-long cylinder. These discrepancies originate from differences in scanner characteristics and phantom shapes. In addition, the measurements by Badawi et al. did not include the effect of activity outside the axial FOV (*11*).

Finally, as we have already noted, the NEC figure of merit allows estimating the statistical quality of the data in the acquisition with regard to the injected dose to the patient. The NEC rate does not account either for inaccurate correction methods of the scattered or random coincidences or for resolution and noise correlation changes introduced by processing and reconstruction of the data. Further studies are required to compare the image quality obtained from 2D and 3D acquisitions, such as human or numeric observer performance studies (*29,30*). This is the purpose of our ongoing work based on the methodology developed for use with volumetric image display (*31,32*).

CONCLUSION

We have measured the NEC rate for 2D and 3D whole-body PET acquisitions using an anthropomorphic phantom. These results have been correlated with clinical data to derive guidelines on the injected patient dose for 2D and 3D acquisitions to maximize NEC rates for the particular PET scanner evaluated here. For the scanner type and whole-body ^{18}F-FDG distribution considered here, the peak NEC rate in 2D mode was not reached within an acceptable range of injected activity, whereas in 3D mode there was a distinct maximum for the NEC rate, for which the corresponding

injected dose depended on patient height and weight. For the brain, the 3D NEC rates were significantly higher than the 2D NEC rates at all activity levels. For the thorax and abdomen, however, there was no clear advantage to either the 2D or the 3D mode. The relative NEC rates depend on the amount of activity present and the local imaging environment. Although knowing the NEC rate as a function of patient dose does not provide all the information needed for protocol optimization, it is a necessary step in that direction.

ACKNOWLEDGMENTS

This study was supported by a grant from Siemens-France (Saint-Denis, France) and by National Institutes of Health grant CA 74135. The authors acknowledge Vincent Brulon and Pascal Merceron for their assistance with the phantom acquisition; Jean Lumbroso, MD, Badia Hélal, MD, Nicolas Delahaye, MD, Hélène Gauthier, MD, and the clinical staff of the Orsay PET facility for their assistance with the clinical data; and David Brasse, PhD, for helpful discussions.

REFERENCES

1. Rigo P, Paulis P, Kaschten BJ, et al. Oncological applications of positron emission tomography with fluorine-18 fluorodeoxyglucose. *Eur J Nucl Med.* 1996;23:1641–1674.
2. Dahlbom M, Hoffman EJ, Hoh CK, et al. Whole-body positron emission tomography. Part I. Methods and performance characteristics. *J Nucl Med.* 1992;33: 1191–1199.
3. Daube-Witherspoon ME, Green SL, Bacharach SL, et al. Influence of activity outside the field-of-view on 3-D PET imaging [abstract]. *J Nucl Med.* 1995; 36(suppl):184P.
4. Bailey DL, Miller MP, Spinks TJ, et al. Experience with fully 3D PET and implications for future high-resolution 3D tomographs. *Phys Med Biol.* 1998;43: 777–786.
5. Strother SC, Casey ME, Hoffman EJ. Measuring PET scanner sensitivity: relating count rates to image signal-to-noise ratios using noise equivalent counts. *IEEE Trans Nucl Sci.* 1990;37:783–788.
6. Brix G, Zaers J, Adam LE, et al. Performance evaluation of a whole-body PET scanner using the NEMA protocol. *J Nucl Med.* 1997;38:1614–1623.
7. Adam LE, Zaers J, Ostertag H, et al. Performance evaluation of the whole-body PET scanner ECAT EXACT HR+ following the IEC standard. *IEEE Trans Nucl Sci.* 1997;44:1172–1179.
8. Bailey DL, Jones T, Spinks TJ, et al. Noise equivalent count measurements in a neuro-PET scanner with retractable septa. *IEEE Trans Med Imaging.* 1991;10: 256–260.
9. Dahlbom M, Cherry SR, Eriksson L, et al. Optimization of PET instrumentation for brain activation studies. *IEEE Trans Nucl Sci.* 1993;40:1048–1054.
10. Stearns CW, Cherry SR, Thompson CJ. NECR analysis of 3D brain PET scanner designs. *IEEE Trans Nucl Sci.* 1995;42:1075–1079.
11. Badawi RD, Marsden PK, Cronin BF, et al. Optimization of noise-equivalent count rates in 3D PET. *Phys Med Biol.* 1996;41:1755–1776.
12. Laforest R, Cutler PD, Daube-Witherspoon ME. Extra shielding for improved signal-to-noise in 3D whole-body PET. *Proceedings of the IEEE Nuclear Science Symposium and Medical Imaging Conference, Seattle, WA, 1999.* Vol 3. Los Alamitos, CA: IEEE; 1999:1359–1362.
13. Smith RJ, Adam LE, Karp JS. Methods to optimize whole body surveys with the C-PET camera. *Proceedings of the IEEE Nuclear Science Symposium and Medical Imaging Conference, Toronto, Canada, 1999.* Vol 3. Los Alamitos, CA: IEEE; 1999:1197–1201.
14. Doshi NK, Basic M, Cherry SR. Evaluation of the detectability of breast cancer lesions using a modified anthropomorphic phantom. *J Nucl Med.* 1998;39:1951–1957.
15. Zasadny KR, Wahl RL. Standardized uptake values of normal tissues at PET with 2-(fluorine-18)-fluoro-2-deoxy-D-glucose: variations with body weight and a method for correction. *Radiology.* 1993;189:847–850.
16. Turkington TG, Williams NE, Hamblen SM, et al. Regional FDG uptake, attenuation, and geometries measurements for whole body phantom design [abstract]. *J Nucl Med.* 1999;40(suppl):281P.
17. Defrise M, Kinahan P. Data acquisition and image reconstruction for 3D PET. In: Bendriem B, Townsend DW, eds. *The Theory and Practice of 3D PET.* Dordrecht, The Netherlands: Kluwer Academic Publishers; 1998:11–54.
18. Cherry SR, Meikle SR, Hoffman EJ. Correction and characterization of scattered events in three-dimensional PET using scanners with retractable septa. *J Nucl Med.* 1993;34:671–678.
19. Bergström M, Eriksson L, Bohm C, et al. Correction for scattered radiation in a ring detector positron camera by integral transformation of the projections. *J Comput Assist Tomogr.* 1983;7:42–50.
20. Barnes D, Egan G, O'Keefe G, et al. Characterization of dynamic 3-D PET imaging for functional brain mapping. *IEEE Trans Med Imaging.* 1997;16:261–269.
21. Sossi V, Pointon B, Boudoux C, et al. NEMA NU 2-2000+ performance measurements on an ADC MCD camera. *IEEE Trans Nucl Sci.* 2001;48:1518–1523.
22. Sorenson JA, Phelps ME. *Physics in Nuclear Medicine.* Orlando, FL: Grune and Stratton; 1987:439.
23. Committees of The American Diabetes Association Inc. *A Guide for Professionals: The Effective Application of Exchange Lists for Meal Planning.* Chicago, IL: The American Dietetic Association; 1977.
24. International Commission on Radiological Protection. *Reference Man: Anatomical, Physiological and Metabolic Characteristics.* Oxford, England: International Commission on Radiological Protection; 1975.
25. Karp JS, Daube-Witherspoon ME, Hoffman EJ, et al. Performance standards in positron emission tomography. *J Nucl Med.* 1991;32:2342–2350.
26. Townsend DW, Isoardi RA, Bendriem B. Volume imaging tomographs. In: Bendriem B, Townsend DW, eds. *The Theory and Practice of 3D PET.* Dordrecht, The Netherlands: Kluwer Academic Publishers; 1998:111–132.
27. Wienhard K, Bailey DL, Bol A, et al. Applications of 3D PET. In: Bendriem B, Townsend DW, eds. *The Theory and Practice of 3D PET.* Dordrecht, The Netherlands: Kluwer Academic Publishers; 1998:133–167.
28. Bailey DL. *Quantification in 3D Positron Emission Tomography* [dissertation]. Surrey, England: University of Surrey; 1996.
29. Metz CE. ROC methodology in radiologic imaging. *Invest Radiol.* 1986;21:720–733.
30. Farquhar TH, Llacer J, Sayre J, et al. ROC and LROC analyses of the effects of lesion contrast, size, and signal-to-noise ratio on detectability in PET images. *J Nucl Med.* 2000;41:745–754.
31. Swensson RG. Unified measurement of observer performance in detecting and localizing target objects on images. *Med Phys.* 1996;23:1709–1725.
32. Lartizien C, Kinahan PE, Comtat C, et al. A tumor detection observer study comparing 2D versus 3D wholebody PET imaging protocols. *Proceedings of the IEEE Nuclear Science Symposium and Medical Imaging Conference, Lyon, France, 2000* [book on CD-ROM]. Los Alamitos, CA: IEEE; 2000.